NASA Contractor Report 198444
ICOMP–96–02; CMOTT–96–01

Transonic Turbulent Flow Predictions With New Two-Equation Turbulence Models

William W. Liou and Tsan-Hsing Shih
Institute for Computational Mechanics in Propulsion and
Center for Modeling of Turbulence and Transition
Cleveland, Ohio

January 1996

Prepared for
Lewis Research Center
Under Cooperative Agreement NCC3–370

National Aeronautics and
Space Administration

ICOMP
Lewis Research Center
Ohio Aerospace Institute

TRANSONIC TURBULENT FLOW PREDICTIONS WITH NEW TWO-EQUATION TURBULENCE MODELS

William W. Liou* and Tsan-Hsing Shih**

Center for Modeling of Turbulence and Transition
ICOMP,NASA Lewis Research Center, Cleveland, Ohio

Abstract

Solutions of the Favre-averaged Navier-Stokes equations for two well-documented transonic turbulent flows are compared in detail with existing experimental data in this paper. While the boundary layer in the first case remains attached, a region of extensive flow separation has been observed in the second case. Two recently developed $k-\varepsilon$, two-equation, eddy-viscosity models are used to model the turbulence field. These models satisfy the realizability constraints of the Reynolds stresses. Comparisons with the measurements are made for the wall pressure distribution, the mean streamwise velocity profiles and turbulent quantities. Reasonably good agreement is obtained with the experimental data.

I. Introduction

In this paper, the accuracy and the range of applicability of two new two-equation turbulence models for transonic shock-wave/boundary-layer interactions are assessed. Generally, when regions of subsonic Mach number and regions of supersonic Mach number both exist in a flow, the flow is said to be transonic. Transonic flow fields may be found in internal flows, for example, in engine compressor passages and external flows, for example, around airfoils. Other than a few exceptional cases, where fluid machines were specifically designed for shock-free compression, the transition from supersonic to subsonic flows invariably occurred through shock waves. The location and the strength of the shock wave impact significantly the characteristics of a fluid machine involving the transonic flow. For example, the major part of the loss associated with a compressor blade passage and the loading on an airfoil are closely related to these factors. Therefore, accurate predictions of transonic flows with embedded shock waves can help improve the efficiency of many important fluid machines. The location and the strength of the shock wave in a transonic flow is determined by the interaction between the shock waves and the boundary layer. With a sufficiently fine grid, modern numerical schemes, such as the various TVD schemes and the new $a-\mu$ scheme[1], etc., can capture the shock wave satisfactorily. Therefore, a successful prediction of such flows hinges largely upon the physical modeling of the interaction process. In this paper, two new eddy-viscosity turbulence models are used to predict transonic turbulent separated flows. These two-equation models, one a low-Reynolds number model and the other a high-Reynolds number model, satisfy the realizability constraints of the Reynolds stresses. The value of the coefficient for the eddy viscosity is determined by the mean flow deformation rate and the turbulence quantities. The models, therefore, can be particularly suitable for flows with large or sudden flow deformation.

Two transonic flows with embedded shock waves are calculated in this paper. In the first, an internal transonic flow field is generated by using floor-mounted, two-dimensional bump models[2], Fig. 1, and the flow is symmetric. The flow was observed to be incipiently separated. The quasi-normal shock extends across the tunnel and the flow is choked. The flow was identified as ONERA Bump A in the EUROVAL effort[3], a program devoted to the validation of computational fluid dynamics (CFD) codes with special attention directed toward the validation of turbulence models. In the second configuration studied here[4], Fig. 2, a circular cylinder aligned with the flow direction is used to generate the external transonic flow field. In this case, the shock, which terminates before reaching the tunnel wall, is sufficiently strong to induce an extensive region of flow separation. The axisymmetric configuration is relatively free from side-wall interference with the turbulent boundary layer and is particularly suitable for the evaluation of model performance in the prediction of strong viscous-inviscid interactions with

---

*Senior Research Associate, Institute for Computational Mechanics in Propulsion. Member AIAA

**Technical Leader, CMOTT, Institute for Comutational Mechanics in Propulsion.

flow separation. This particular flow was also selected as a test case for transonic separated flows in the 1980 AFSOR–HTTM–Stanford conference[5] and was identified as Case 8611.

These two cases, although relatively simple, contain fundamentally essential characteristics that are important in the design process of, for example, wings, engine compressors and turbines. Therefore, successful predictions of these flows can have profound industrial importance.

To provide an objective comparison of the model performance, care has been taken to obtain solutions on sufficiently refined computational grids so that the observed difference in the results can be attributed directly to the turbulence models used in the calculations.

In the following sections, the turbulence models and the numerical platform used in this study are described. The results of flow calculations are then compared with those obtained by using two existing two–equation models, e.g., Chien's model[6] (CH) and the standard $k-\varepsilon$ model (SKE).

II. Analysis

Mean Flow Equations

The flow properties are decomposed into two parts: a mean value and a fluctuation with respect to the mean value. That is,

$$\hat{\rho} = \rho + \rho'' \tag{1.a}$$

$$\hat{u}_i = U_i + u_i' \tag{1.b}$$

$$\hat{p} = p + p'' \tag{1.c}$$

$$\hat{T} = T + T' \tag{1.d}$$

$$\hat{E} = E + E' \tag{1.e}$$

where ρ, p, T, E, U_i denote Reynolds-averaged density and pressure, mass-weighted-averaged temperature, total energy, and velocity, respectively. It is customary to use both the Reynolds average and the mass-weighted average in the decomposition process for compressible turbulent flows to simplify the final form of the mean flow equations. The governing equations for the mean flow may be obtained by substitution of flow properties in the form of eq.(1) into the Navier-Stokes equations followed by a Reynolds average of the equations. The mean flow equations become,

$$\rho_{,t} + (\rho U_i)_{,i} = 0 \tag{2.a}$$

$$(\rho U_i)_{,t} + (\rho U_i U_j + \tau_{ij} + p\delta_{ij})_{,j} = 0 \tag{2.b}$$

$$(\rho E)_{,t} + (\rho U_i E + pU_i + q_{T,i} + \tau_{ij} U_j + q_{k,i})_{,i} = 0 \tag{2.c}$$

where

$$\tau_{ij} = 2(\mu + \mu_t) S_{ij} - \frac{2}{3} k \delta_{ij}$$

μ denotes the mean molecular viscosity and S_{ij} denotes the mean strain rate tensor, i.e.,

$$S_{ij} = \frac{1}{2}(U_{i,j} + U_{j,i}) - \frac{1}{3} U_{k,k} \delta_{ij} \tag{3}$$

The turbulent Reynolds stresses are modeled via the turbulent eddy viscosity, μ_t. In all of the models used in this study, the turbulent eddy viscosity is determined by the turbulent kinetic energy, k, and the dissipation rate, ε, i.e.,

$$\mu_t = C_\mu f_\mu \rho \frac{k^2}{\varepsilon} \tag{4}$$

k and ε are obtained from the solution of their respective model transport equations. f_μ is the wall damping function for the eddy–viscosity. For reference, these models are described briefly in the following.

Turbulence Models

In Shih *et. al*[7], a general constitutive relation between the Reynolds stresses and the mean flow deformation rate was derived by using the invariance principle of Lumley. The model satisfies the realizability constraints: for example, the energy component $\overline{u_1 u_1}$ should always be positive. Note that the standard $k-\varepsilon$ model with $C_\mu = 0.09$ is an unrealizable model. For example, $\overline{u_1 u_1}$ becomes negative when

$$\frac{S_{11} k}{\varepsilon} > \frac{1}{0.27}. \tag{5}$$

Therefore, the value of C_μ should not be a constant for a realizable model. In Shih *et. al*[7], the realizability constraints have led to,

$$C_\mu = \frac{1}{A_0 + A_s U^{(*)} \frac{k}{\varepsilon}} \tag{6}$$

where

$$U^{(*)} = \sqrt{S_{ij} S_{ij} + \bar{\Omega}_{ij} \bar{\Omega}_{ij}}$$
$$\bar{\Omega}_{ij} = \tilde{\Omega}_{ij} - 2\epsilon_{ijk}\omega_k$$
$$\tilde{\Omega}_{ij} = \Omega_{ij} - \epsilon_{ijk}\omega_k$$

Ω_{ij} is the mean rotation rate viewed in a rotating reference frame with the angular velocity ω_k. The parameter A_s is determined by

$$\begin{aligned} A_s &= \sqrt{6}\cos\phi, \quad \phi = \frac{1}{3} arc\cos(\sqrt{6}W) \\ W &= \frac{S_{ij} S_{jk} S_{ki}}{\bar{S}^3} \quad \bar{S} = \sqrt{S_{ij} S_{ij}} \end{aligned} \tag{7}$$

The new formulation of C_μ, with an explicit dependence on the mean strain rate, can be used to render a model realizable. It is also in accord with the experimental observation that the value of C_μ can be different for different flows. The value of A_0 is set equal to 4.0[8]. It is determined by examining the log–law of the inertial sublayer. The corresponding value of C_μ is 0.09. As was noted by Shih *et. al*[8], the resulting formulation for C_μ also worked very well for homogeneous shear flows. The first model tested here is the Shih and Lumley model[9], modified by including the new formulation of C_μ (Yang *et. al*[10]). The second model by Shih *et. al*[8], on the other hand, has applied the variable C_μ formulation during the development of the model.

A: Shih and Lumley Model[9] – KE1

The model equations for k and ε in KE1 model are,

$$\rho k_{,t} + \rho U_i k_{,i} = [(\mu + \mu_t) k_{,i}]_{,i} - \rho \widetilde{u_i u_j} U_{i,j} - \rho\varepsilon \quad (8.a)$$

$$\begin{aligned}\rho\varepsilon_{,t} + \rho U_i \varepsilon_{,i} = {} & [(\mu + \frac{\mu_t}{\sigma_\varepsilon})\varepsilon_{,i}]_{,i} - C_1 \frac{\varepsilon}{k} \rho \widetilde{u_i u_j} U_{i,j} \\ & - C_2 f_2 \rho \frac{\varepsilon^2}{k} + \nu \mu_t U_{i,jk} U_{i,jk}\end{aligned} \quad (8.b)$$

where

$$C_1 \doteq 1.44, \quad C_2 = 1.92, \quad \sigma_\varepsilon = 1.3$$

$$f_2 = 1 - 0.22\exp[-(\frac{R_t}{6})^2], \quad R_t = \frac{k^2}{\nu\varepsilon}$$

The damping function is defined by

$$f_\mu = [1. - \exp(-(a_1 R_k + a_3 R_k + a_5 R_k))]^{\frac{1}{2}} \quad (9)$$

where

$$a_1 = 1.7 \times 10^{-3}, \quad a_3 = 10^{-9}, \quad a_5 = 5 \times 10^{-10}$$

$$R_k = \frac{\rho\sqrt{k}y}{\mu}$$

Note that the value a_1 has been modified due to the application of the new formulation of variable C_μ which is bounded by 0.09 in the current application. This modified Shih and Lumley model[9] has been shown to predict well a variety of flows in Yang *et. al*[10]. The near–wall boundary conditions for the turbulent quantities are determined by examining the Kolmogorov behavior of near-wall turbulence proposed by Shih and Lumley[9]. They have shown that energetic eddies reduce to "Kolmogorov eddies" at a finite distance from the wall and all the wall parameters are characterized by Kolmogorov microscales. Therefore, an estimate can be obtained for the turbulent kinetic energy and its dissipation rate at the location where large eddies become Kolmogorov eddies by using both direct numerical simulation results and an asymptotic analysis of near wall turbulence. According to their analysis, this turbulent limit point is located at

$$y_\eta = \frac{6\nu}{u_\tau} \quad (10)$$

At this limit point,

$$k_\eta = 0.25 u_\tau^2 \quad \text{and} \quad \varepsilon_\eta = 0.251 \frac{u_\tau^4}{\nu} \quad (11)$$

In practice, the boundary conditions are enforced at the wall. With the application of eqns.(10) and (11), the turbulent time scale near a wall, similar to the velocity and length scales, is determined by the Kolmogorov time scale. Therefore, there is no unphysical singularity in the current model ε equation.

B: Shih *et. al* Model[8] – KE2

A new form of model equation for the turbulent dissipation rate was proposed by Shih *et. al*[8]. The equation for the mean-square vorticity fluctuation was first examined by using an order of magnitude analysis. The truncated low-order equation is then modeled through physical reasoning. The modeled equation for the mean-square vorticity fluctuation can be transformed into an equation for the turbulent dissipation rate in the limit of high Reynolds number. The resulting model equation for ε is,

$$\rho\varepsilon_{,t} + \rho U_j \varepsilon_{,j} = [(\mu + \frac{\mu_t}{\sigma_\varepsilon})\varepsilon_{,j}]_{,j} + C_1 \rho S\, \varepsilon - C_2 \rho \frac{\varepsilon^2}{k + \sqrt{\nu\varepsilon}} \quad (12)$$

where

$$C_1 = max\{0.43, \quad \frac{\eta}{5+\eta}\}, \quad \sigma_\varepsilon = 1.2, \quad C_2 = 1.9$$

$$S = \sqrt{2 S_{ij} S_{ij}}, \quad \eta = \frac{Sk}{\varepsilon}$$

In Shih *et. al*[8], the new modeled dissipation rate equation has been coupled with the standard model equations for k, eq.(8.a), to form a two–equation model. Because $\sqrt{\nu\varepsilon}$ appears in the denominator of the sink term, this new dissipation rate equation will not become singular even if k vanishes. C_μ is defined by eq.(6). Near the wall, a compressible wall-function was applied.

$$\frac{u}{u_\tau} = \frac{1}{\kappa} ln(y^+) + C \quad (13)$$

u is the Van Driest transformed velocity defined as,

$$u = \sqrt{B}[arcsin(\frac{A+U}{D}) - arcsin(\frac{A}{D})] \quad (14)$$

where

$$A = \frac{q_w}{\tau_w}, \quad B = \frac{2c_p T_w}{Pr_t}, \quad D = \sqrt{A^2 + B}$$

The heat flux near the wall is defined as,

$$q = q_w + U\,\tau \tag{15}$$

The turbulent quantities are defined as,

$$k = \frac{\tau_w/\rho}{\sqrt{C_\mu}}, \qquad \varepsilon = \frac{(\tau_w/\rho)^{3/2}}{\kappa y} \tag{16}$$

The value of $y^+ (= u_\tau y/\nu_w)$ for the first grid point away from the wall, where the wall-function is applied, is about 30. Although the validity of the wall-function boundary conditions in complex separated flows is somewhat ambiguous, previous work seems to show that it can provide reasonably accurate predictions for a wide range of flows[11,12].

It should be noted that except for the mean flow volume dilatation, no explicit compressibility effect models have been included in any of the models in the calculations performed in this study.

The results of calculations using these two realizable models, which are presented in a later section, have been compared with those obtained by using the standard $k-\varepsilon$ model (SKE) and Chien's (CH) low-Reynolds number $k-\varepsilon$ model. The SKE and CH models are representative of the high- and low-Reynolds number types of model, respectively. They are chosen here for comparison due to their simplicity and stability. In the following, the numerical solution procedure is described.

III. Numerical Solutions

The Favre-averaged Navier-Stokes equations and the model transport equations have been solved numerically by using the COMTUR code developed by Huang and Coakley[13]. Briefly, it uses a line-by-line Gauss-Seidel algorithm and Roe's approximate Riemann solver. Yee's MINMOD TVD scheme was applied in all the computations. The mean and the turbulence equations are solved in a sequential manner. All the calculations have been carried out with the same initial and boundary conditions, including those for k and ε.

Since the model bump mounted on the top wall is the same as the one mounted on the bottom wall, see Fig. 1, only the lower half of the channel is computed in ONERA Bump A. Symmetry conditions were imposed along the centerline of the channel. The chord length of the floor bump is 0.2 m. The computational domain extends from 0.5 chords upstream of the leading edge ($x = 0$) of the bump to 0.128 m downstream of the trailing edge of the bump. At the computational inlet, the stagnation conditions were prescribed and the mean velocity in the transverse direction was assumed zero. At the exit, the back pressure was prescribed. Mass conservation was also ensured at the exit. For Case 8611, the bump is 20.32 cm in length (=C). The computational domain extends from -2C to 3.5C. At the computational inlet, the known experimental stagnation conditions and the flow Mach number (=0.875) were prescribed. For both cases, low levels of turbulent kinetic energy and dissipation rate were prescribed at the inlet.

The computational domains were covered with non-orthogonal surface-fitted meshes, with grid clustering at the shock location and near the wall. Several different meshes were used to ensure grid-independence, by varying both the number of grid nodes and the grid clustering. For ONERA Bump A, it was found that the isentropic wall Mach number changed by less than 0.2% for two grids (180×60 and 160×60). For low-Reynolds number models, a mesh of 180×70 nodes was found sufficient to provide a grid-independent solution. Similarly, for Case 8611, 180×70 for the models employing wall-function and 180×80 for the low-Reynolds number models were found sufficient to ensure grid-independence. About forty to fifty grid points are typically located inside the boundary layer. In the following section, the solutions obtained with the fine meshes are presented.

IV. Results and Discussions

In this section, the results obtained by using KE1 and KE2 models are presented and compared with the experiments.

ONERA Bump A

As was mentioned earlier, at the exit the back pressure was imposed. With the experimental value of 0.641 (P/P_T), it was found that the predicted shock locations were different. Consequently, the models' capability in predicting the flow structures in the interaction region can be obscured due to their difference in predicting the shock locations. To obtain a meaningful comparison of the model predictions, it has been suggested [3] that the experimental exit pressure be perturbed for the individual model so that the calculated isentropic wall Mach number on the bump wall is 1.047 at x=0.158 m. This allows a fair comparison of the model predictions of the interaction process without any influence resulting from a mismatch of the shock location. The computed centerline Mach numbers have been compared with the measurement and are shown in Fig. 3. With the adjusted exit pressure, the computed and measured shock locations agree well. The computed shocks are quite sharp, reconfirming the ability of the TVD scheme in capturing shock waves in the inviscid region. The two high-Reynolds number models, SKE and KE2 models, predicted slightly higher post-shock expansion than the two low-Reynolds number models, CH and KE1 models, in the immediate post-shock region. All of them, however, lie below the the measurement. This appears to indicate three-dimensional effects related to the thickening of the boundary layers on the side-wall of the wind tunnel, causing the acceleration of the flow in the center of the channel.

Figure 4 shows the comparison of the predicted and measured wall pressure distributions. KE2 model shows the best agreement with the measured values in the post-shock region, followed by SKE, KE1, and CH models. All the model predictions of the wall pressure asymptote to a value higher than the measurement.

Figure 5 shows the predicted and measured distributions of the boundary-layer displacement thickness on the bump wall. A method proposed by Stock and Haase[14] has been used in determining the displacement thickness. Overall, the low-Reynolds number CH and KE1 models return fairly good agreement with the measurement. SKE and KE2 models predict higher peak values, suggesting a greater sensitivity to the shock. The larger displacement of the boundary layer predicted by the SKE and KE2 models in the immediate post-shock region has led to the lower wall pressure, Fig. 4, or higher isentropic wall Mach number. In the recovery region, all the models show excessive boundary-layer displacement. This suggests that the models would return higher centerline Mach numbers and lower wall pressures than the measurements, which are not observed in Figs. 3 and 4. Since the experimental flow is confined in the spanwise direction, this apparent inconsistency may also be attributed to the three-dimensional effects mentioned earlier.

Measured and computed streamwise mean velocity profiles are shown in Fig. 6. The model predictions agree well with the measured profiles upstream of the interaction region, x=0.15 m. The mean velocity profiles in the interaction region, say, x=0.155 m and x=0.16 m, were found very sensitive to the shock locations. Downstream of this region, all the models give reasonable predictions of the mean velocity profiles.

In Fig. 7, the Reynolds shear stress predictions are compared with the data. The shear stress profiles upstream and downstream of the interaction region have been reasonably well predicted by all the model. In the interaction region, the turbulent Reynolds shear stress were not well predicted. It should be noted, however, that experimental uncertainly can be higher for measuring stresses than for mean velocity. Also, the turbulent structures are more sensitive to shocks than is the mean flow.

Case 8611

A sketch of the flow is shown in Fig. 2. The experiment has shown a large region of flow separation immediate downstream of the shock due to the effects of shock/turbulent boundary-layer interaction and the geometry of the floor model. As noted earlier, this flow configuration is particularly suitable for the study of transonic turbulent separated flows, since the axisymmetric flow model provides a flow that is relatively free from three-dimensional and tunnel wall effects. In fact, the experiments have been repeated later in a larger facility and the reported changes in the shock locations are within 1% chord. The data were acquired at a freestream Mach number of 0.875. At this Mach number, the flow separates at $x/C \approx 0.7$ and the reattachment occurs at $x/C \approx 1.1$. The griding of the computational domain is basically the same as those in the previous case. Again, the fine grid solutions are presented.

Figure 8 shows the Mach number contours using the SKE model. The increment between the contour lines is a constant value of 0.05. A supersonic pocket is formed above the bump surface and the shock has been captured very well. The shock is curved, suggesting that the computational mesh is sufficiently fine.

The measured and the computed surface pressure distributions are compared in Fig. 9. The KE2 model's prediction on a coarser grid (160×60) has also been shown for comparison. There is no significant difference between the fine- and coarse-grid solutions. The high-Reynolds number KE2 model gives the best prediction of the wall pressure near the shock location. The shock predicted by the CH model is located downstream of the experimental shock. In the region of flow separation, the CH model underestimates the level of the viscous/inviscid interaction and gives the highest pressure rise among all the models tested. Compared with the CH model, the KE1 model has shown a significant improvement. The KE2 model predicts rather well the wall pressure in this region. This model also shows a significant improvement over the SKE model. To quantify the comparison, at the trailing edge of the bump, x/C=1, the differences between the predicted and measured wall pressure are about 1.6%, -0.1%, 4.3%, and 2.8% for the KE1, KE2, CH, and SKE models, respectively.

Comparisons of the computed and measured streamwise mean velocity profiles are shown in Fig. 10. The model predictions agree reasonably well with the measurements upstream of the interaction region, x/C=0.563. In the region of flow separation, x/C=0.75, 0.875, and 1.0, The KE2 model seems to predict a boundary layer that is more sensitive to the effect of the shock than the other models tested and the CH model gives slightly better predictions. The KE2 model has predicted a faster flow recovery than the other models. Figure 11 shows the computed and measured Reynolds shear stress profiles. Near the shock wave, x/C=0.75, the KE2 model has correctly predicted the peak value of the Reynolds shear stress. The predicted location of the peak, however, is slightly higher than the measurement. Further downstream, the flow predicted by the KE2 model relaxes rather quickly. At x/C=1.375, the KE2 model has predicted a better profile distribution and peak level predictions than the other models. The turbulent kinetic energy profiles are compared in Fig. 12. In the interaction region, the KE2 model overpredicts the location of the peak turbulence energy. Due to the relatively fast flow recovery predicted by the KE2 model, however, the KE2 model predictions of the turbulent kinetic energy agree far better than the other models downstream of the immediate region of strong interaction. Figure 13 shows the distributions of the eddy–viscosity coefficient, C_μ, ahead, amid, and behind the interaction region. For the CH and SKE models, the value has a constant value of 0.09. For the KE1 and KE2 models, its value depends on the local mean and turbulent flow field. At x/C=0.563, the value of C_μ given by KE2 model is different from 0.09, indicating the fact that the flow has been affected by the bump. The distribution at x/C=0.75 shows that the KE1 and KE2 models react rather differently to the shock/turbulent boundary–layer interaction process. Since there is no upper limit when the variable C_μ formulation is used with the KE2 model, the maximum value of C_μ is about 0.25, which occurs when either the mean strain rate or the turbulence energy vanishes. As is shown in Fig. 13, this occurs in the outer part of boundary layer from x/C=0.875 to 1.375.

V. Summary

Two new realizable, $k-\varepsilon$, eddy–viscosity models have been assessed in the calculations of two transonic flows with weak and strong shock/turbulent boundary-layer interactions. For calculations with the same type of models, i.e., high- vs. low–Reynolds number models, the same initial, boundary conditions and computational meshes were used.

For the weak interaction case, the two new realizable models perform better than the selected existing models of the same type. The performance differences, however, are not significant. For the case with strong shock/turbulent boundary–layer interactions, the high–Reynolds number model of Shih *et. al*[8] has shown the greatest sensitivity to the interaction process and given a far better prediction for the wall pressure distribution and the shock location than the other models tested. In addition, the two high–Reynolds number models tested here, i.e., the Shih *et. al*[8] model and the standard $k-\varepsilon$ model, have predicted better overall performance than the two low–Reynolds number models.

Acknowledgements

The authors would like to thank Dr. P.G. Huang at MCAT Inc. Mountain View, CA, for helpful discussions and comments.

References

[1] Chang, S.-C., "The method of space–time conservation element and solution element–A new approach for solving the Navier–Stokes and Euler equations," To appear in *J. Comp. Phys.* (1995).

[2] Delery, J. and Reisz, J., "Analyse experimentale d'une interaction choc-couche limite turbulente a Mach 1.3 (decollment naissant)" ONERA Rapport Technique No. 42/7078 AY 014, Chatillon, December 1980.

[3] *EUROVAL-A European Initiative on Validation of CFD Codes.* Edt. W. Haase, F. Bradsma, E. Elsholz, M. Leschziner and D. Schwanborn, 1992.

[4] Bachalo, W. D. and Johnson, D. A., "Transonic, turbulent boundary-layer separation generated on an axisymmetric flow model," *AIAA Journal*, **24**, 437–443 (1986).

[5] The 1980–81 AFSOR–HTTM–Standford Conference on Complex Turbulent Flows: Comparison of Computaion and Experiment. Edited by S. J. Kline, BJ. J. Cantwell, and G. M. Lilley (1981).

[6] Chien, K.-Y., "Predictions of channel and boundary layer flows with a low Reynolds number turbulence model," *AIAA Journal*, **20**, 33-38 (1982).

[7] Shih, T. H., Zhu, J., and Lumley, J. L., "A new Reynolds stress algebraic equation model," NASA TM 106644 (1994). Accepted for publication in *Comput. Methods Appl. Mech. Eng.*.

[8] Shih, T. H., Liou, W. W., Shabbir, A., Yang, Z., and Zhu, J., "A new $k-\varepsilon$ eddy viscosity model for high Reynolds number turbulent flows," *Computers Fluids*, **24**, 227-238 (1995).

[9] Shih, T. H. and Lumley, J. L., "Kolmogorov behavior of near–wall turbulence and its application in turbulence modeling," *Comp. Fluid Dyn.*, 1, 43-56 (1993).

[10] Yang, Z., Georgiadis, N., Zhu, J., and Shih, T.-H., "Calculations of inlet/nozzle flows using a new $k-\epsilon$ model," AIAA paper 95–2761 (1995).

[11] Huang, P. G. and Coakley, T. J., "Calculations of supersonic and hypersonic flows using compressible wall functions," Second International Symposium on Engineering Turbulence Modeling and Measurement, Florence, Italy, 1993.

[12] Huang, P. G. and Liou, W. W., "Numerical calculations of shock–wave/boundary–layer flow interactions," NASA TM 106694 (1994).

[13] Huang, P. G. and Coakley, T. J., "An implicit Navier–Stokes code for turbulent flow modeling," AIAA paper 92-0547 (1992).

[14] Stock, H. W. and Haase, W., "Determination of length scales in algebraic turbulence models for Navier–Stokes methods," *AIAA Journal*, 27, 5–14 (1989).

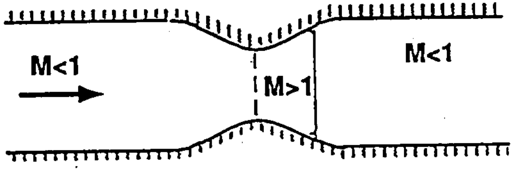

Figure 1. A sketch for ONERA Bump A.

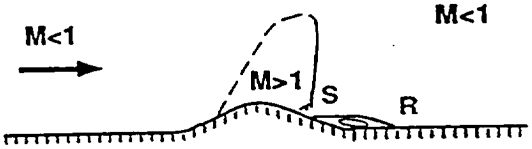

Figure 2. A sketch for Case 8611.

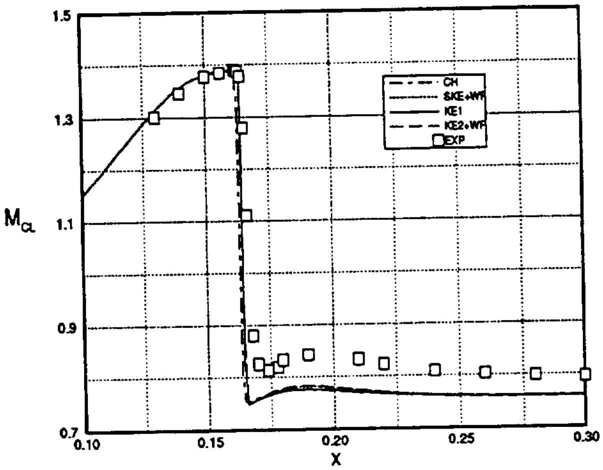

Figure 3. Variation of Mach number along the centerline. ONERA Bump A

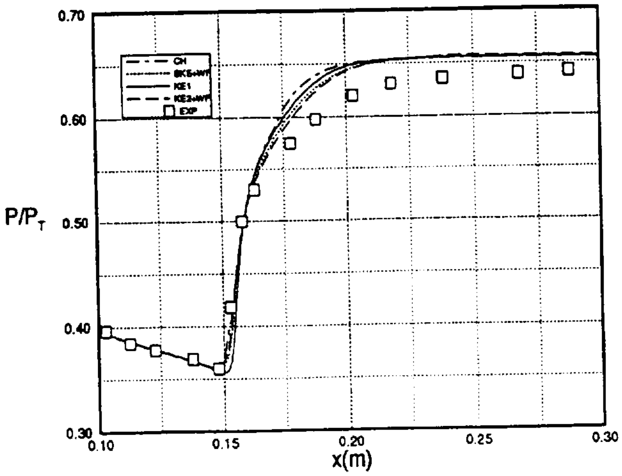

Figure 4. Variation of isentropic wall Mach number. ONERA Bump A

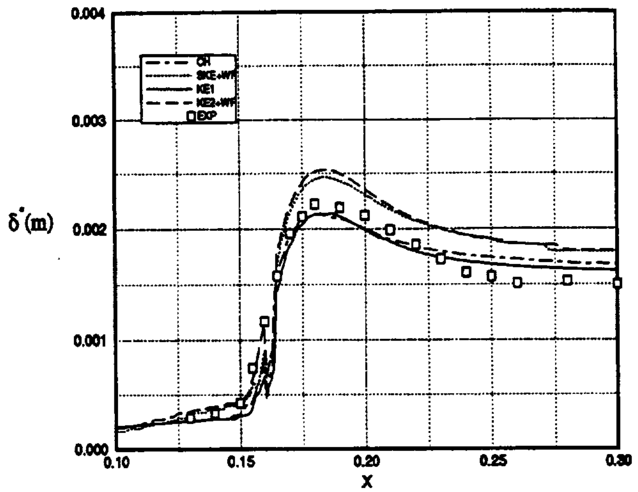

Figure 5. Variation of boundary-layer displacement thickness. ONERA Bump A

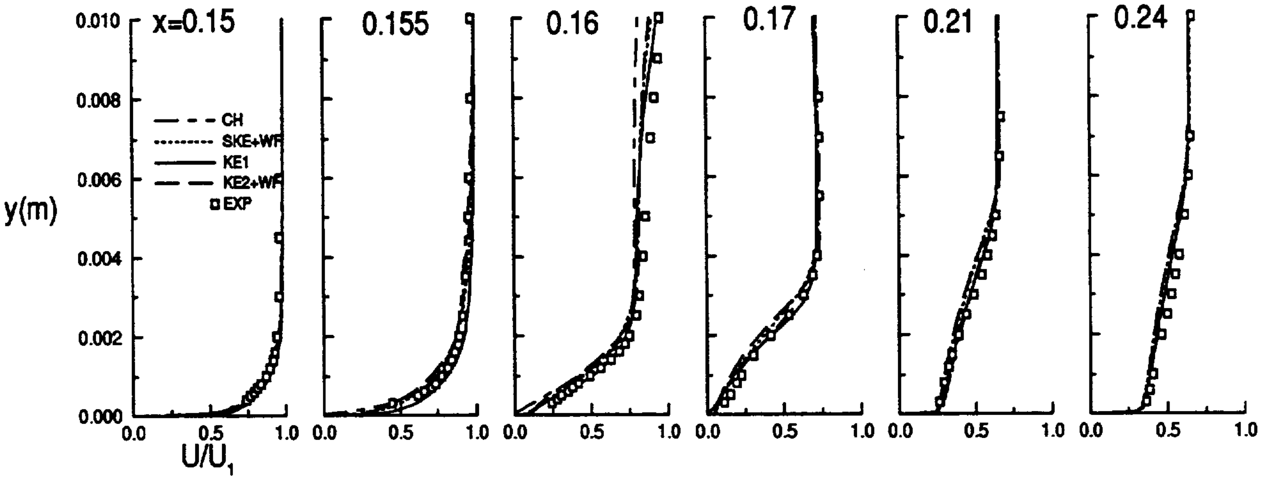

Figure 6. Streamwise mean velocity profiles. ONERA Bump A.

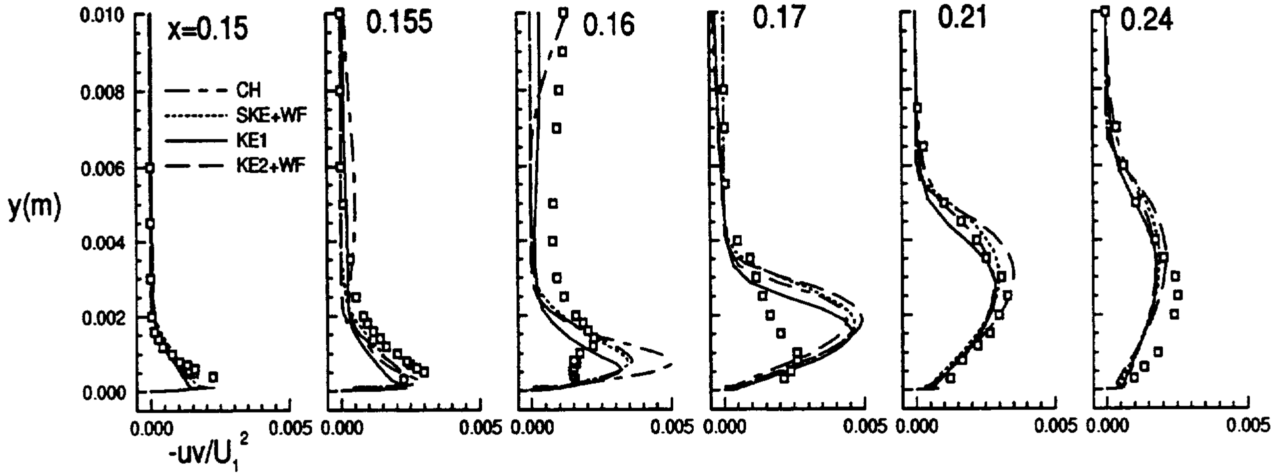

Figure 7. Comparison of Reynolds shear stress profiles. ONERA Bump A.

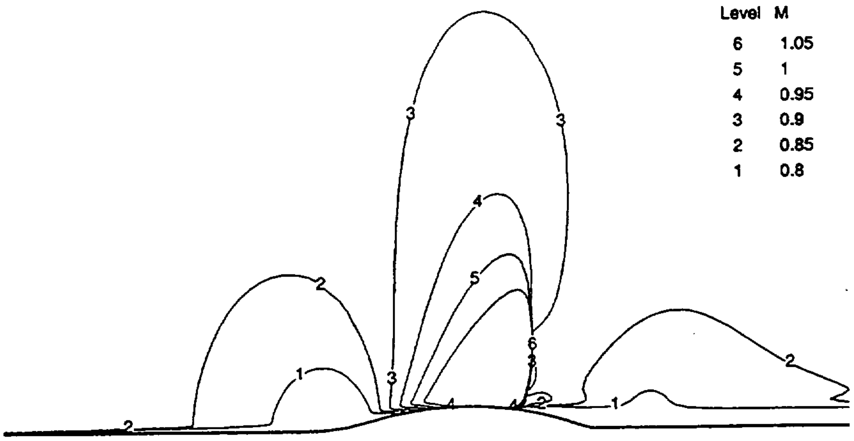

Figure 8. Mach number contours. Case 8611.

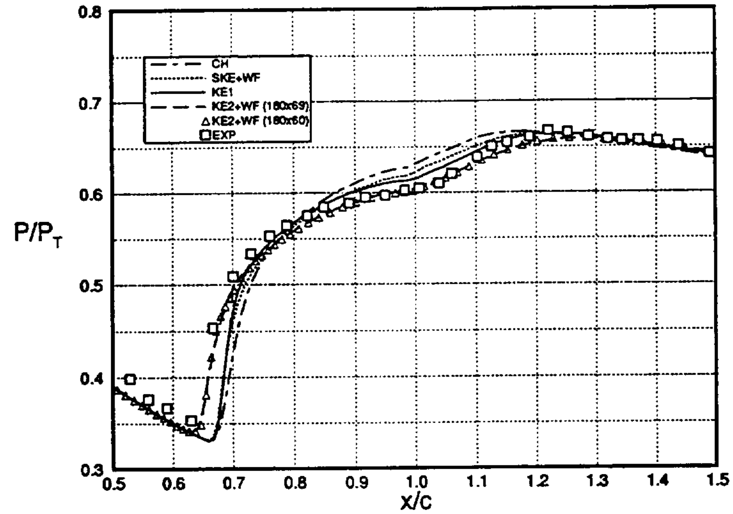

Figure 9. Variation of wall pressure. Case 8611.

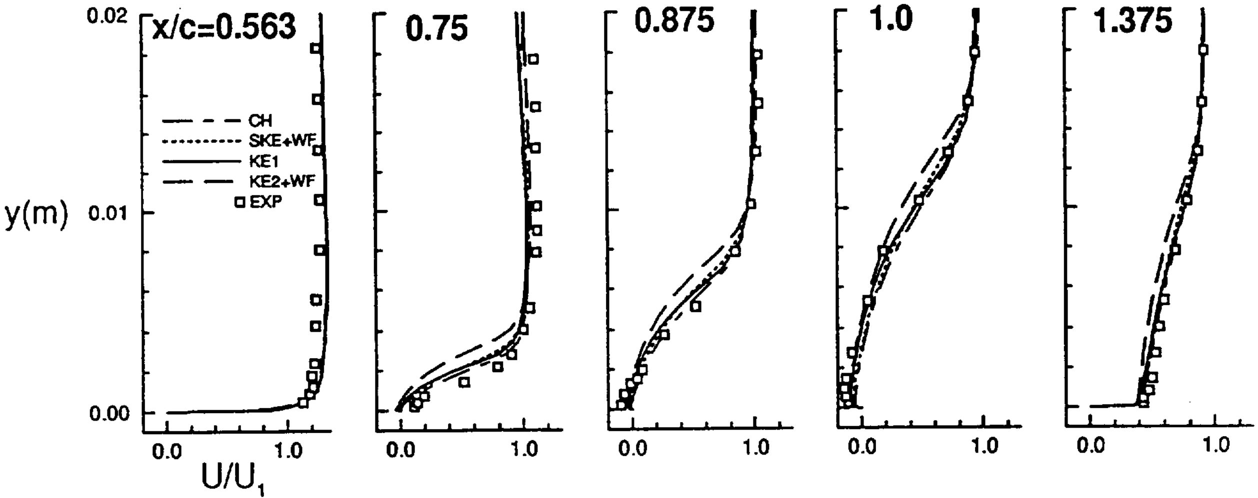

Figure 10. Streamwise mean velocity profiles. Case 8611

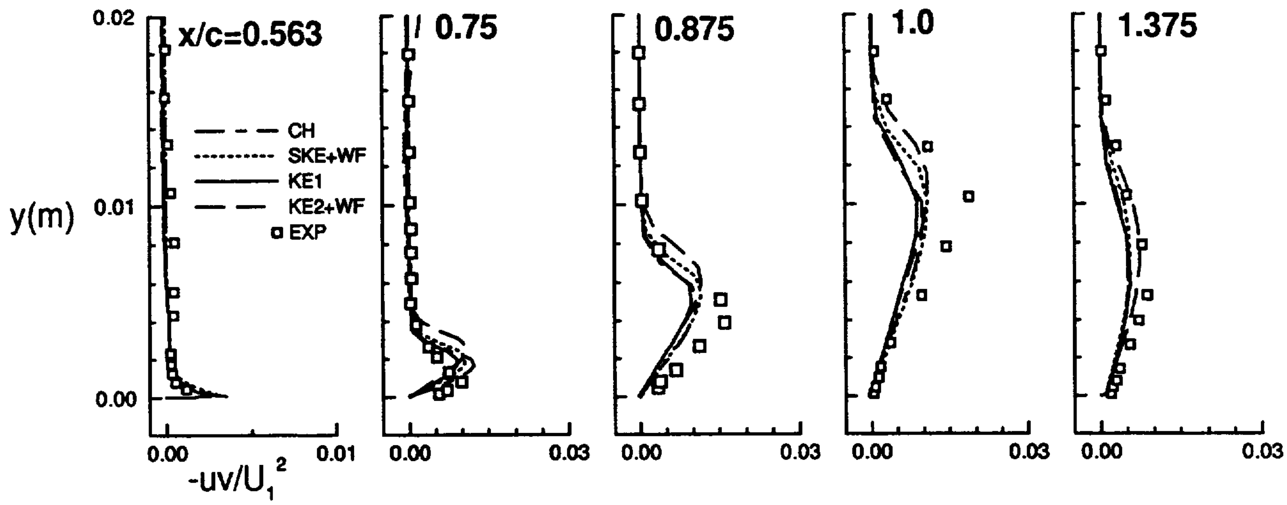

Figure 11. Reynolds shear stress profiles. Case 8611

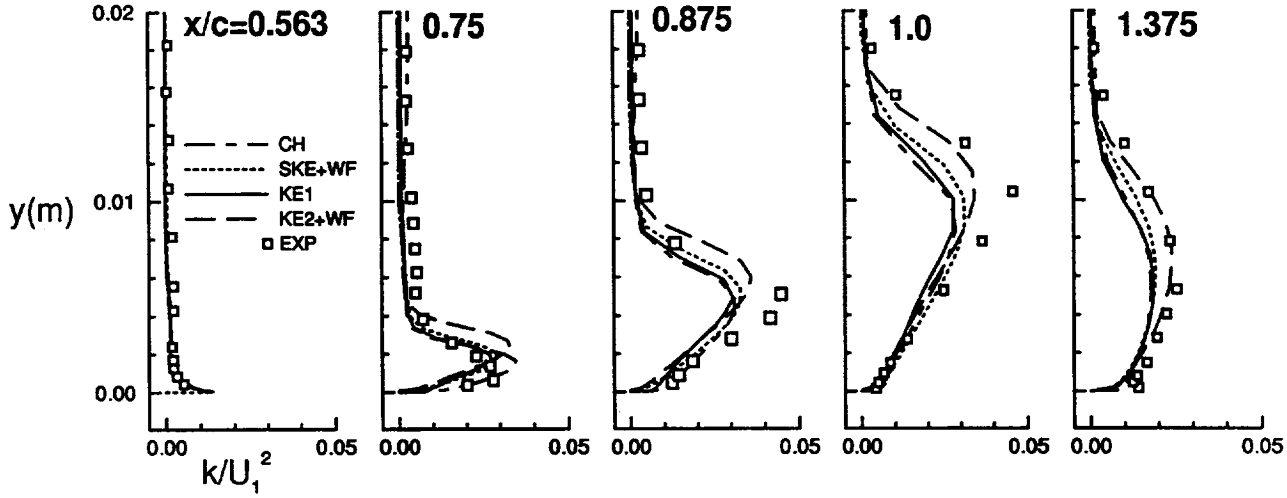

Figure 12. Turbulent kinetic energy profiles. Case 8611

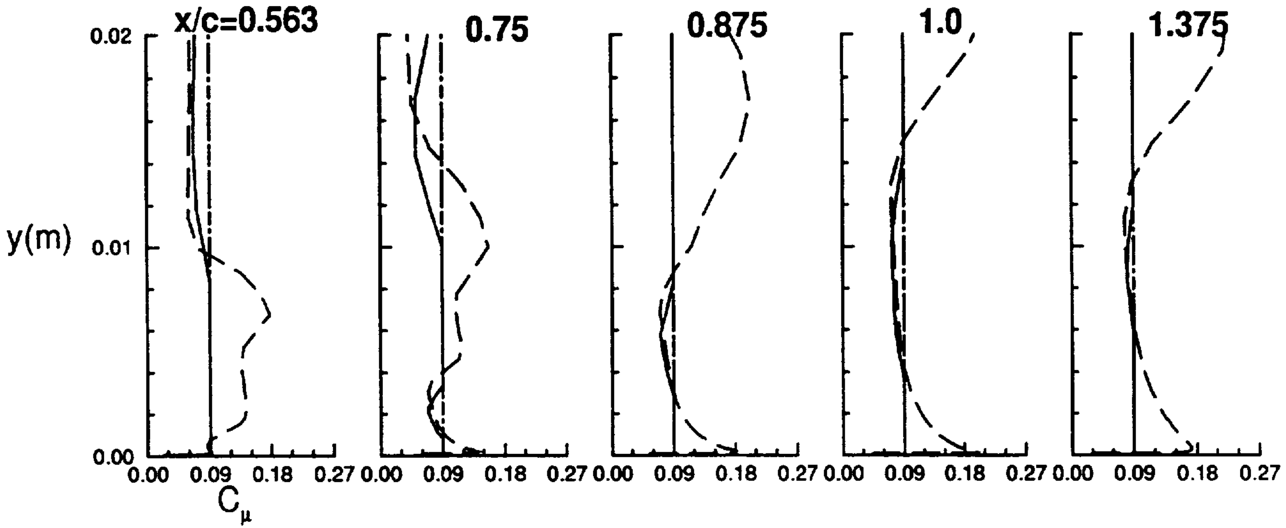

Figure 13. Comparison of C_μ. Case 8611. Legend: see Figure 11.

REPORT DOCUMENTATION PAGE

Form Approved
OMB No. 0704-0188

1. AGENCY USE ONLY *(Leave blank)*	**2. REPORT DATE** January 1996	**3. REPORT TYPE AND DATES COVERED** Contractor Report

4. TITLE AND SUBTITLE Transonic Turbulent Flow Predictions With New Two-Equation Turbulence Models	**5. FUNDING NUMBERS** WU-505-90-5K NCC3-370
6. AUTHOR(S) William W. Liou and Tsan-Hsing Shih	
7. PERFORMING ORGANIZATION NAME(S) AND ADDRESS(ES) Institute for Computational Mechanics in Propulsion 22800 Cedar Point Road Cleveland, Ohio 44142	**8. PERFORMING ORGANIZATION REPORT NUMBER** E-10083
9. SPONSORING/MONITORING AGENCY NAME(S) AND ADDRESS(ES) National Aeronautics and Space Administration Lewis Research Center Cleveland, Ohio 44135-3191	**10. SPONSORING/MONITORING AGENCY REPORT NUMBER** NASA CR-198444 ICOMP-96-02 CMOTT-96-01

11. SUPPLEMENTARY NOTES

Prepared for the 13th Applied Aerodynamics Conference sponsored by the American Institute for Aeronautics and Astronautics, San Diego, California, June 19–22, 1995. ICOMP Program Director, Louis A. Povinelli, organization code 2600, (216) 433-5818.

12a. DISTRIBUTION/AVAILABILITY STATEMENT Unclassified - Unlimited Subject Category 34 This publication is available from the NASA Center for Aerospace Information, (301) 621-0390.	**12b. DISTRIBUTION CODE**

13. ABSTRACT ***(Maximum 200 words)***

Solutions of the Favre-averaged Navier-Stokes equations for two well-documented transonic turbulent flows are compared in detail with existing experimental data in this paper. While the boundary layer in the first case remains attached, a region of extensive flow separation has been observed in the second case. Two recently developed $k-\varepsilon$, two-equation, eddy-viscosity models are used to model the turbulence field. These models satisfy the realizability constraints of the Reynolds stresses. Comparisons with the measurements are made for the wall pressure distribution, the mean streamwise velocity profiles and turbulent quantities. Reasonably good agreement is obtained with the experimental data.

14. SUBJECT TERMS Transonic turbulent flows; Turbulence modeling	**15. NUMBER OF PAGES** 12
	16. PRICE CODE A03

17. SECURITY CLASSIFICATION OF REPORT Unclassified	**18. SECURITY CLASSIFICATION OF THIS PAGE** Unclassified	**19. SECURITY CLASSIFICATION OF ABSTRACT** Unclassified	**20. LIMITATION OF ABSTRACT**

National Aeronautics and
Space Administration
Lewis Research Center
Cleveland, OH 44135-3191
ICOMP OAI